Effect of Weld Characteristic on Mechanical Strength of Laser-Arc Hybrid-Welded Al-Mg-Si-Mn Aluminum Alloy

CHEN ZHANG, MING GAO, MING JIANG, and XIAOYAN ZENG

Laser-arc hybrid welding (LAHW) was employed to improve the tensile properties of the joints of 8-mm-thick Al-Mg-Si-Mn alloy (AA6082) using Al-5Mg filler wire. The weld microstructures were examined by scanning electron microscope, electron backscattered diffraction, and transmission electron microscopy in detail. The LAHW joints with pore-free and high-tensile performances were obtained. The strength enhancement of the fusion zone and heat-affected zone in the LAHW joint was mainly attributed to the grain refinement strengthening and the precipitation strengthening, respectively. The microstructure characteristics were related to the effects of laser-arc interaction on the energy transfer within the molten pool. The arc caused the majority of laser energy to dissipate out of the keyhole, and then it reduced the heat input. The lower heat input refined the grain size, weakened the overaging effect, and thus improved the tensile strength.

I. INTRODUCTION

PRECIPITATION-HARDENED Al-Mg-Si-Mn aluminum (Al) alloy (AA6082-T6) is a heat-treatable reinforced alloy. It has been widely used in a high-speed train vehicle structure for its preferable properties of low density, high specific strength, and favorable plasticity.[1] Since the assembling of the high-speed railway vehicle car-body depends on welding entirely, the rapid development of the high-speed rail network, especially in China, demands new welding techniques to obtain higher welding speed and better welding quality.

Some modified MIG welding and friction stir welding (FSW) have been studied for this aim.[2,3] During MIG welding, bigger heat input easily coarsens or dissolves the Mg2Si' phases or Mn-containing dispersoids in the weld, which significantly decreases the joint strength.[4] FSW also has shortcomings, such as geometrical constraints, low welding speed, root flaws due to the lack of tool penetration, and high force to react against the welding tool pressure load.[2] It makes the FSW of a thick-walled structure less efficient.

Laser-arc hybrid welding (LAHW) is now one of the most promising types of fusion welding because it combines the advantages of both laser welding and arc welding, such as deeper penetration depth, faster welding speed, and better welding quality. This new welding technique has garnered more and more attention in the past decade and has been successfully used in the manufacturing of steel structures, such as ship decks, car bodies, and oil pipelines.[5,6] Some studies have addressed Al alloys with a thickness of less than 5 mm. The results showed that compared with MIG welding, the LAHWed Al joints were 85 pct less thermal distortion, had a fine microstructure, and had 10–20 pct higher tensile properties.[7–13] However, no reports have been done on LAHWed Al joints with a thickness above 5 mm because LAHW of thick Al alloys faces more challenges.

First, the suppression of weld porosity becomes more difficult, and the difficulty increases with the increase of the thickness. During LHAW or laser welding of Al alloys, the weld porosity is mainly caused by the collapse of unstable laser keyhole and hydrogen gas bubbles.[14,15] The deeper the laser keyhole, the unstable the laser keyhole, and the easier the formation of weld pores.[16] During LAHW, the arc pressure can accelerate the escape of the bubbles from the molten pool to the air by enlarging the molten pool and the driving force of melt flow, prolonging the solidification.[17,18] However, the effect of arc pressure is limited to the shallow area due to the low-energy density of the arc. For the thick plates, the arc effect becomes ineffective because the laser key hole is too deep. It means that the LAHWed joints of thick Al alloys, especially Al-Mg-Si alloys, is hard to obtain, so few reports have addressed the LAHW of thick Al alloys so far. The literature[8] has shown that the AlSi5 filler has the ability to remove the porosity of an 8-mm-thick Al-Mg-Si alloy LAHWed joint because the Si element can improve the fluidity of molten pool. However, the excess Si content in Al-Mg-Si alloys would decrease the mechanical properties,

CHEN ZHANG, Lecturer, is with the School of Mechanical & Electrical Engineering, Wuhan Institute of Technology, Wuhan 430205, P.R. China, and also with the Wuhan National Laboratory for Optoelectronics, Huazhong University of Science and Technology, Wuhan 430074, P.R. China. MING GAO and XIAOYAN ZENG, Professors, and MING JIANG, Lecturer, are with the Wuhan National Laboratory for Optoelectronics, Huazhong University of Science and Technology. Contact e-mail: jm_china@hust.edu.cn

especially the toughness and the fatigue strength because of the generation of lots of Al-Mg$_2$Si and Al-Si eutectic structures, which is unacceptable for the safety of a train vehicle.

Second, the balance of the microstructure and the mechanical properties of the LAHW joint should be considered. Current studies have shown that the strengths of LAHWed Al-Mg-Si alloy joints were up to 74–80 pct of the base metal (BM), which is far higher than those of other fusion welding.[14,19–24] Casalino et al. found that the higher cooling rate of LAHW could refine the microstructure such as the dendrite arm spacing.[14] Yan et al. claimed that the precipitate coarsening and the element vaporization caused the loss of strength in the joint.[24] Other factors, such as grain size, grain orientation, and the dislocations, also play a big role in determining the mechanical properties of the Al joint.[25–27] However, those factors have been scarcely studied in the LAHW of Al alloys.

How to obtain a thick Al alloy weld with excellent mechanical properties and without welding defects is a challenge for LAHW. By a series of experiments on LAHW of 8-mm-thick AA6082-T6 alloy, we have achieved the accepted joints with pore-free and higher tensile properties, which has not been reported elsewhere. During the experiments, high arc current was employed. Usually, the big heat input generated from high arc current would deteriorate the mechanical properties by coarsening the microstructure. However, it is encouraging that the tensile strength of LAHWed joints obtained in this article was improved greatly, which solves the two challenges mentioned earlier. To understand the microstructure–property relationship in the LAHW of Al alloy, this article aims to discuss the strengthening mechanisms by laser-arc interaction.

II. EXPERIMENTAL METHOD

Commercial AA6082-T6 Al alloy with a thickness of 8 mm and ER5087 filler wire with a diameter of 1.6 mm were employed in this study. The chemical compositions of BM and filler wire are listed in Table I. An IPG YLR-6000 fiber laser with a wavelength of 1070 nm was employed. The maximum output power is 6 kW, the beam quality parameter is 6.9 mm × m rad, and the beam mode is TEM$_{01}$ (transverse electromagnetic mode). The laser beam was transferred to the welding head through an optical fiber with a 200-μm core diameter and focused by a 250-mm lens. The focus spot diameter of the laser beam is 0.4 mm. An arc welding machine is Fronius TPS4000 with a maximum electric current of 400 A. Reference 22 gives the welding preparation and the arrangement of the laser beam and arc torch. Where the distance between the focus spot of laser beam and the tip of filler wire was 3 mm, and the angle between the incident laser beam and the vertical line is 5 deg, the tilt angle of the arc torch to the workpiece surface was 60 deg. The melt pool surface was observed using a PCO high-speed video camera (photography speed: 4500 f s^{-1}) and Cavitar pulse fiber laser lighting source, and their spatial positions were as shown in Figure 1. To prevent laser and molten material leakage, a backing was placed under the base material. The welding parameters optimized in previous studies are listed in Table II. Comparisons were made between LAHW, laser welding, and arc welding at the same parameters.

After welding, the transverse tensile strength of the joints was first tested according to ISO 4136-2001. The strength of a weld is the average value of three specimens. Because some specimens fractured in the heat-affected zone (HAZ), a U groove sample was designed to test the tensile strength of the fusion zone (FZ).[17] The U groove, which is a semicircle with a 2 mm radius, was machined in the FZ, as shown in Figure 2. The as-received tensile fractures were examined using a FEI Sirion 200 scanning electron microscope (SEM) operated at an accelerating voltage of 15 to 20 kV.

The metallographic samples were prepared by polished by emery paper and anti-scuffing paste, and then they were etched by HF solution (2 vol pct). The macrostructure of the transverse cross section of the welds was observed by a NIKON optical microscope (OM). Because the backing was irradiated and melted by the laser beam, its transverse cross section was also observed by OM. The dendrite microstructure was characterized by OM. The grain structure was analyzed by electron backscattered diffraction (EBSD) integrated in the SEM. The crystallographic data were processed by the enclosed software in the SEM. The grain size was measured according to the lineal intercept procedure by reference to ASTM E112 (Standard Test Methods for Determining Average Grain Size). The elongated grain size was divided into lengthwise and widthwise. The EBSD specimens were prepared by electropolishing in a 10 pct perchloric acid in alcohol solution at a voltage of 20 V for 30 seconds. Compositional analysis of the weld was carried out by energy-dispersive X-ray spectroscopy (EDS) integrated with the SEM at 20 kV. The precipitate and dislocation were studied by a FEI Tecnai G2 F30 transmission electron microscope (TEM) operated at 300 kV. TEM specimens were prepared by jet polishing using a mixed solution of nitric acid (33 vol pct) and methanol (67 vol pct) at 253 K and 12 V.

III. RESULTS AND DISCUSSIONS

A. Weld Cross-Section Morphologies

As shown in Figures 3(a) through (c), the arc current of those joints increases in order, as well as the corresponding heat input. The increasing arc current or heat input smoothens the transition of the weld profile between the upper and the lower parts. Figure 4 gives the typical high-speed photographs of the molten pool surface of different welding techniques. Compared with pure laser welding or arc welding, a large pit appears at the rear of the keyhole in the LAHW. The depth of the pit increases as arc current. This phenomena was also observed by another study.[28] It indicates that more heat input or melted filler wire is transferred

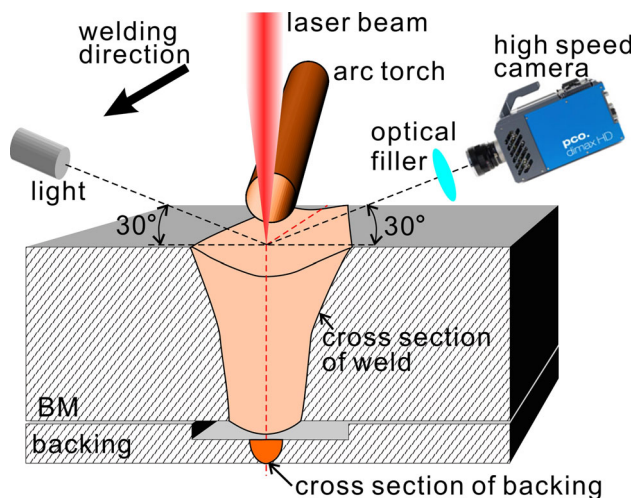| Element	Si	Mg	Cu	Mn	Fe	Cr	Zn	Ti	Zr	Al
BM (AA6082-T6)	0.96	0.8	0.10	1.0	0.50	0.25	0.20	0.10	—	bal.
Wire (ER5087)	0.04	4.76	0.01	0.75	0.14	0.007	0.01	0.08	0.11	

Fig. 1—Schematic arrangements of imaging system for observation of melt pool.

to the lower part by the larger arc current, which causes a smoother weld profile transition. Moreover, it was found that the backing is melted during LAHW, as shown in Figures 3(d) and (e). It indicates that the laser beam reaches and melts the backing after it penetrates the BM. The big aspect ratio of the melted zone in the backing suggests that the keyhole welding is generated. Comparison between Figures 3(d) and (f) shows that the weld penetration in the backing of laser welding is lower than that of LAHW, which means less laser beam power irradiates on the backing.

B. Tensile Strength

As shown in Figure 5, for the standard tensile samples, both the ultimate tensile strength (UTS) and the yield strength (YS) increase with the decrease of heat input when the arc current is 300 A. Joint 3 has the highest UTS and YS, which are up to 246 and 200 MPa, respectively. This UTS reaches 80 pct of the BM. The strengths of the joints are irregular when the arc current is lower than 300 A. Despite less heat input, these joints' strengths are lower than joint 3. The reason will be discussed in the next section. Since some standard samples were fractured in the HAZ, the U-groove samples of the strongest joint 3 were prepared for evaluating the tensile strength of the FZ. The UTS and the YS of U-groove joint 3 are 270 and 217 MPa, respectively. Table III shows that the optimized UTS and YS of the MIG welded AA6082-T6 joint are about 233 and 180 MPa, respectively.[3,29–31] It indicates that the tensile strengths of the LAHWed joint, especially the

YS, increases dramatically compared with the MIG joints.

C. Fractograph

As shown in Figure 6, several big pores appear on the fracture surfaces of joints 4–9 that appear at the FZ of the standard sample. Big pores decrease the tensile strength, which explains that these joints with less heat input have weaker strength than joint 3. In addition to the lower arc voltage, the lower wire filling rate can also produce more pores. The lower wire filling rate in MIG means lower welding arc current. It causes a smaller molten pool and driving force of molten flow, which hinders the pores from overflowing the molten pool. More pores were produced in these joints.

Figure 7 shows the fracture surfaces of the strongest joint 3. No pores appear on its surfaces. The HAZ is characterized by numerous equiaxial dimples, while the FZ is featured by smaller dimples with some secondary phases. The fractograph of the FZ shows that the size of the secondary phases is 0.5–1 μm, which is larger than that of the precipitation. The EDS analysis shows that the molar ratio of the Mg atom to the Si atom in the secondary phases is about 2, indicating that they are Mg_2Si phases. These Mg_2Si phases might form in the nonequilibrium rapid solidification during welding. Because the amount of the secondary phases is small, the Mg_2Si phases of the FZ are inessential for tensile strength.

D. Weld Microstructure

Figure 8 shows the microstructure of joint 3. There is a partial melted zone (PMZ) with about 200 μm width near the edge of the FZ. The FZ is composed of the columnar dendrite near the fusion line and the equiaxed dendrite in the center. The secondary dendrite arm spacing of the columnar dendrite and equiaxed dendrite were 5–20 μm, which were less than that of arc welding. Considering the effects of the crystal microstructures on the mechanical property, the SEM-EBSD and TEM analyses were employed to examine more details of the crystal microstructure.

The EBSD images of joint 3 are given in Figure 9 to reveal the crystal orientation characteristics. The inverse pole figure (IPF) map shows that the average grain size of the MIG joint is about 96 μm with the same parameter for LAHW joint 3. The average grain size of the equiaxed zone in the FZ is about 50 μm. The grain size of the LAHWed joint is smaller than that of MIG joints. The pole figure (PF) in Figure 10(f) shows that the density peak of the FZ is dispersing and that the

Parameters	Samples									Arc	Laser
	1	2	3	4	5	6	7	8	9		
Laser power, P (kW)	5.5	6	6	5.5	6	6	5.5	6	6	—	6
Wire filling rate, r (m min^{-1})	9.5	9.5	9.5	7.6	7.6	7.6	5.8	5.8	5.8	9.5	—
Mean arc current, I (A)	300	300	300	240	240	240	180	180	180	300	—
Mean arc voltage, U (V)	22.6	22.6	22.6	21.4	21.4	21.4	19.4	19.4	19.4	22.6	—
Welding speed, v (m min^{-1})	1.3	1.5	1.7	1.3	1.5	1.7	1.3	1.5	1.7	1.7	1.7
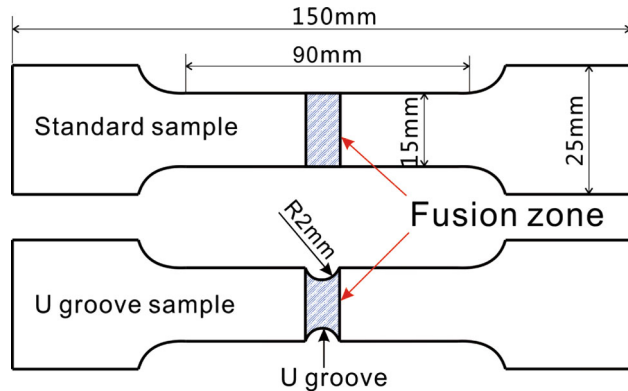
Fig. 2—Schematic drawings of standard and U-groove tensile samples.

highest pole density is only 2.588 times than the random background. It indicates that the grain orientation of the equiaxed zone in the FZ is nearly random. However, the pole density peak of the columnar grain zone in the FZ, as shown in Figures 9(c) and (g), is obviously concentrated, and the highest value is 6.954 times than the random background. It denotes that this region has a microtexture. During welding, with the BM as its nucleus, the columnar grain close to the liquid–solid interface grows preferentially along the direction of the highest temperature gradient, and then it forms the microtexture. Figures 9(d) and (h) show that the overaging zone of the HAZ is composed of rod-like grains with the average size of 5 μm width $\times$ 20 μm length, in which the grain orientation is random and the microtexture is weak. Since no continuous texture appears in the HAZ and the center of the FZ, and the microtexture in the columnar dendrites of the FZ is not parallel to the tensile direction, it can be deduced that the microtexture
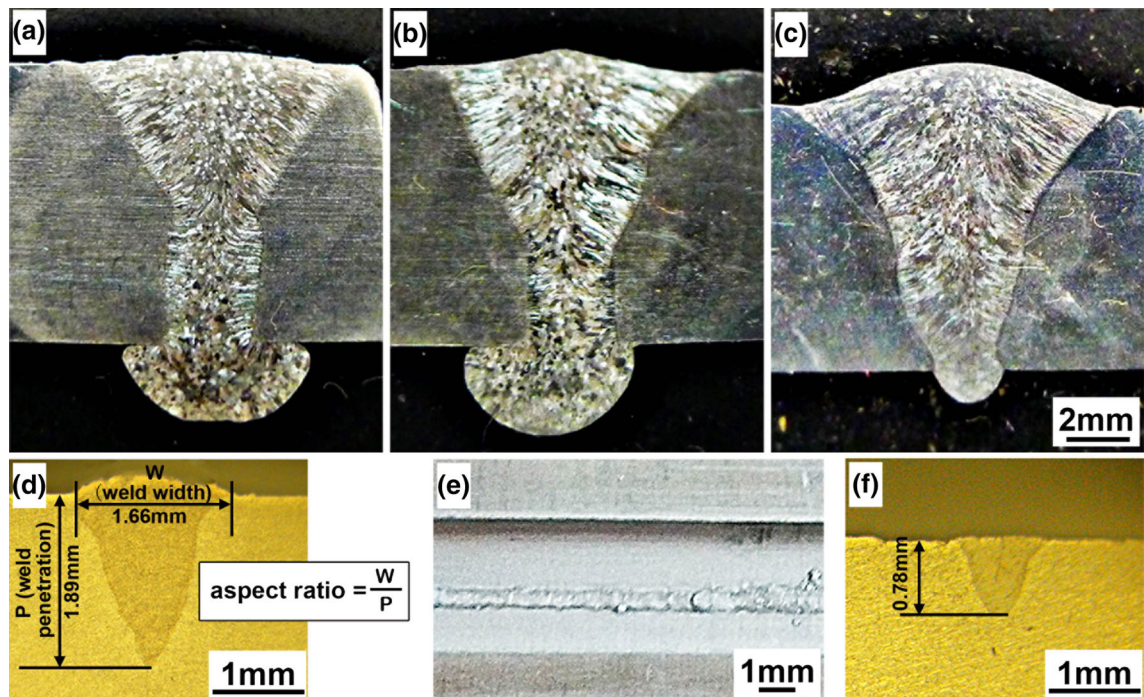

Fig. 3—Cross-section morphologies of LAHWed joints and the morphologies of backing: (a) joint 9, (b) joint 6, (c) joint 3, (d) cross section of backing in LAHW for joint 3, (e) surface of backing in LAHW for joint 3, and (f) cross section of backing in laser welding at the same parameters of LAHW for joint 3.
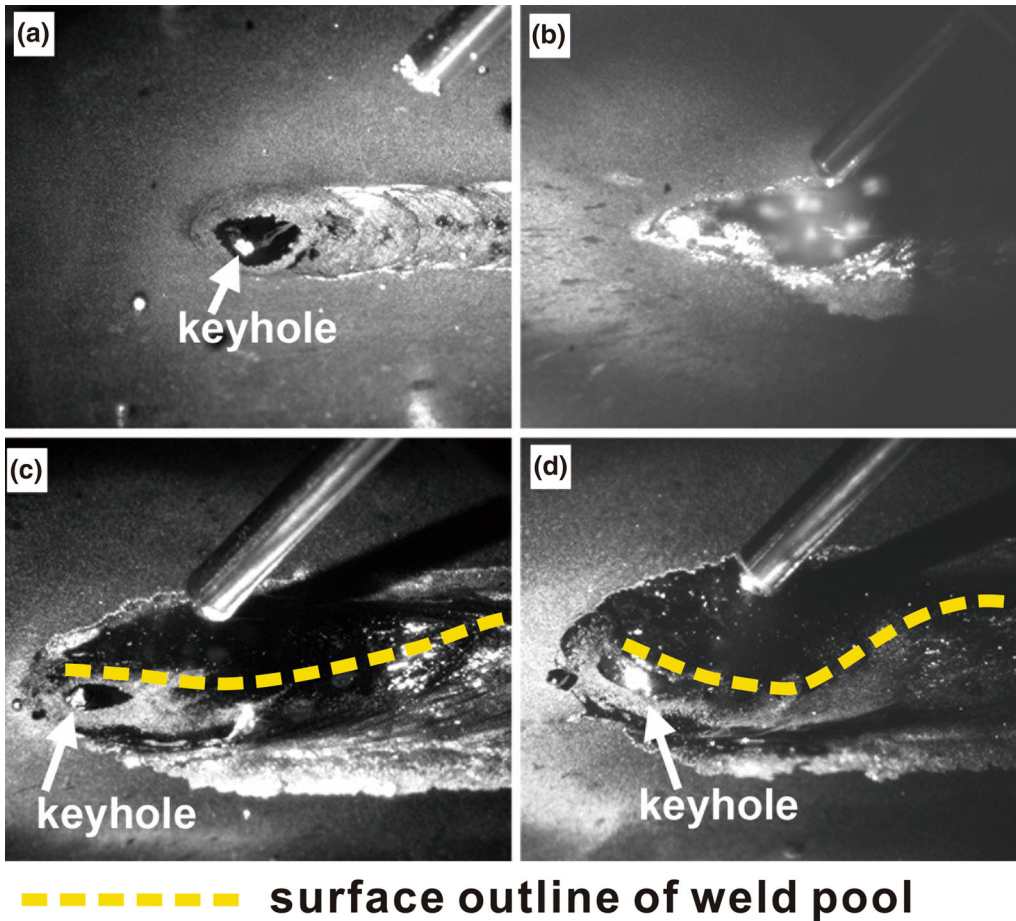
Fig. 4—High-speed photographs of molten pool: (a) laser welding with the parameters of $P = 6$ kW and $v = 1.7$ m min^{-1}, (b) arc welding with the parameters of $I = 300$ A and $v = 1.7$ m min^{-1}, (c) LAHW of joint 9, and (d) LAHW of joint 3.
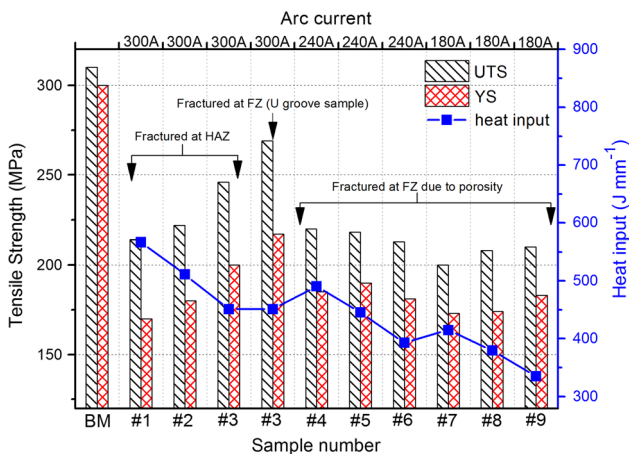

Fig. 5—Tensile strength of standard samples and U-groove sample.

is not the factor improving the tensile strength of the LAHWed joint.[32]

Figure 10 shows the bright field TEM microstructures of BM, FZ, and HAZ in a joint. Some precipitates are found in the BM, and they are inferred as needle-shaped Mg$_2$Si precipitates (typically about 7 nm width × 200 nm length) and coarse Mn-containing dispersoids

(about 100 nm diameter), which usually appear in Al-Mg-Si-Mn alloy.[33,34] As shown in Figure 10(b), there are fine and less pin-dot-like precipitates (about 10 nm) in the FZ, known as GP-I or β″.[35] Figures 10(c) and (d) exhibit the dissolution of the needle-shaped Mg$_2$Si precipitates and the appearance of the coarse spherical precipitates. The element mapping shows that the coarse spherical precipitates are Mn-containing dispersoids. The rod-shaped precipitates in Figure 10(d) are the coarsened needle-shaped Mg$_2$Si precipitates. These different types of precipitates are all able to increase the strength.[34,36]

E. Correlation Between Microstructure and Tensile Strength

The microstructures, as mentioned, such as precipitates and grain, have great effects on the tensile strength of the LAHWed joint. Reference 37 demonstrated that the YS of the welded joint could be presented as the sum of the values from different strengthening methods, and it could be calculated as follows:

$$\sigma_{YS} = \sigma_0 + \sigma_{HP} + \sigma_P + \sigma_{SS} \qquad [1]$$

where σ_{YS} is the YS of the welded joint, σ_0 is the YS of the Al-matrix that is about 10 Mpa,[38] σ_{HP} is the YS

Table III. Tensile Strengths of LAHW Joint Comparison with MIG

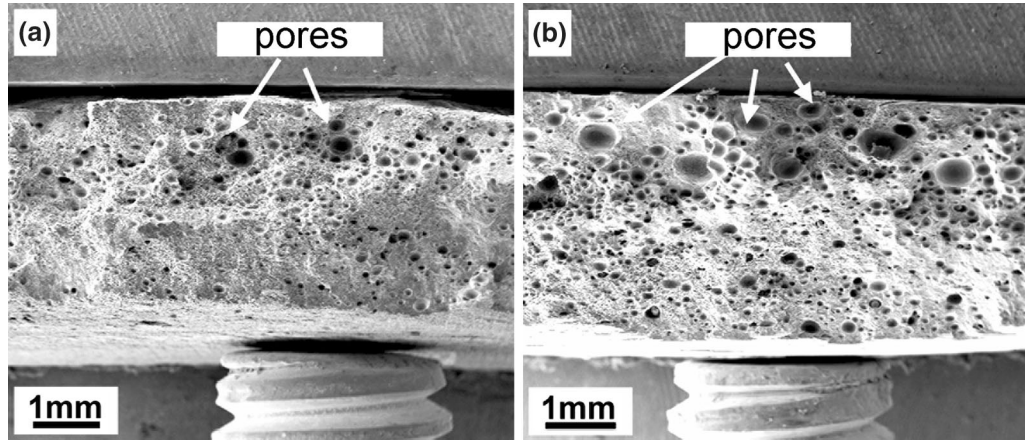| Process	YS (MPa)	UTS (MPa)	Thickness of BM (mm)	Heat Input (J mm^{-1})	Position of Failure	References
LAHW	217	270	8	451.06	FZ	present study
LAHW	200	246	8	451.06	HAZ	present study
MIG	147	221	4	460	HAZ	Ref. [30]
MIG	135	233	13	900	HAZ	Ref. [31]
AC MIG	180	220	1	22.45	FZ	Ref. [29]
Twin wire MIG	—	226	6	377.75	FZ	Ref. [3]

Fig. 6—Fracture surfaces of the typical joints fractured at the FZ, where a large number of pores appear: (*a*) joint 6 and (*b*) joint 9.
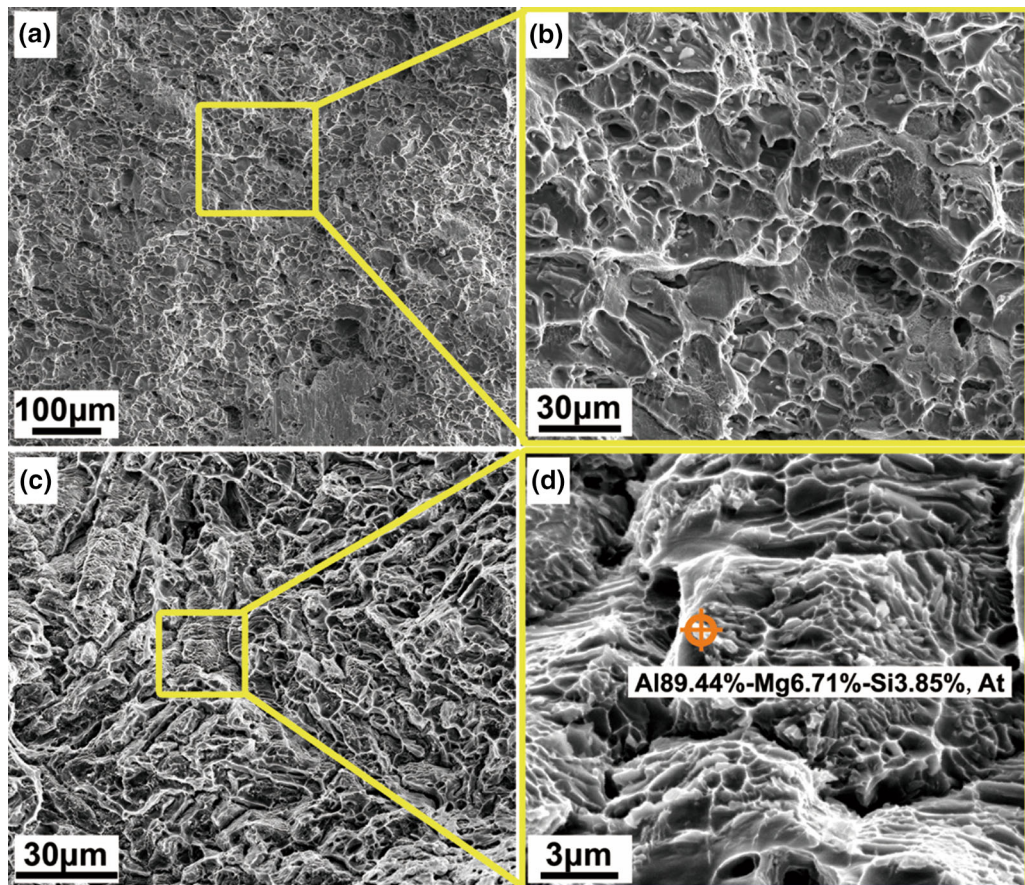

Fig. 7—Fracture surfaces of joint 3 with the highest tensile performance: (*a*) standard sample fractured at the HAZ, (*b*) high magnification of the rectangle in (*a*), (*c*) U-groove sample fractured at the FZ, and (*d*) high magnification of the rectangle in (*c*).

related to grain refinement strengthening, σ_P is the YS related to precipitate strengthening, and σ_{SS} is the YS related to solution strengthening. According to Eq. [1], the correlation between the YS and the microstructure can be established to understand the strengthening mechanism of the LAHWed joint.

The Hall–Patch equation can be used to calculate the YS caused by grain refinement strengthening. Genevois applied it to Al alloys successfully. It is expressed as follows:[37]

$$\sigma_{HP} = \sigma_e + \frac{k}{\sqrt{d}} \qquad [2]$$

where σ_e is the flow stress that is about 20 MPa;[39] k is the constant to describe the relative strength of grain boundary, whose value is 0.17 MPa m$^{1/2}$ for Al-Mg alloys;[38] and d is the grain size of the material. Because the standard and the U-groove tensile samples broke in the overaging zone of HAZ and the central FZ, grain sizes in the overaging zone and the central FZ should be adopted to calculate σ_{HP} of HAZ and FZ, respectively. The EBSD data in Figure 9 show that the average grain sizes of the central FZ and the overaging zone of the HAZ are 50 μm and 5 μm width × 20 μm length, respectively. Thus, according to Eq. [2], the contribution of grain refinement strengthening to the YS of the FZ is 44 MPa. The rod-like grains of HAZ cause anisotropy of the mechanical property, and the contribution to the HAZ is 96 MPa in width and 50 MPa in length.

Based on the theory that the precipitation strengthening depends on the obstruction of precipitates to dislocation movement, Orowan proposed a theoretical equation to calculate the YS of Al alloys caused by precipitation strengthening:[38]

$$\sigma_P = \frac{2.6\,Gb}{\lambda} \qquad [3]$$

where λ is the average spacing between the precipitates, G is the shear modulus of the Al-matrix that is about 26 GPa, and b is Burger's vector of dislocation whose value of Al is 2.84×10^{-10}. The TEM images in Figure 8 show that the λ of the FZ and the overaging zone of the HAZ are about 252 and 138 nm, respectively. According to Eq. [3], the contributions of precipitation strengthening to the strengths of the FZ and the overaging zone of the HAZ are 76 and 140 MPa, respectively.

Kendig had demonstrated that the solid solution strengthening of Al-Mg alloy can be approximated by the following equation:[38]

$$\sigma_{SS} = \frac{3.1\varepsilon Gc^{1/2}}{700} \qquad [4]$$

where ε is the experiment constant and c is the atomic percentage of the solid solution element in the Al-matrix. The chemical compositions of the ER5087 filler wire, as shown in Table I, show that the main solid solution element of the FZ is Mg. It indicates that the solid solution strengthening of the FZ is mainly caused by the element of Mg. Generally, the ε of Mg is 3.8×10^{-7}, and the atomic percentage of Mg in the Al-matrix

measured by EDS is about 3.8 pct. According to Eq. [4], the contribution of solid solution strengthening to the strength of the FZ is 85 MPa. In addition, the solid solution strengthening of the overaging zone of the HAZ is negligible because there are few solid solution elements.

Table IV presents the results calculated earlier. The calculated transverse YSs of the FZ and the HAZ are 200 and 215 MPa, respectively. Both calculations are consistent with the experimental data. According to the calculated data, the solid solution strengthening has the biggest contribution to the YS of the FZ and is a key factor that strengthens the FZ. Since both the LAHWed joint and the arc-welded joints using Al-Mg filler wire have the solid solution strengthening and the precipitation strengthening, the finer grain size of the LAHW joint over the MIG joint suggests that grain refinement strengthening would be the main reason for improving the tensile strength of the LAHWed joint. It indicates that the LAHW has lower heat input than does the MIG welding.

The contributions of precipitate strengthening to the YS of the HAZ are the highest. These data demonstrate that the LAHW process prevents excessive overaging, which means lower heat input in LAHW.
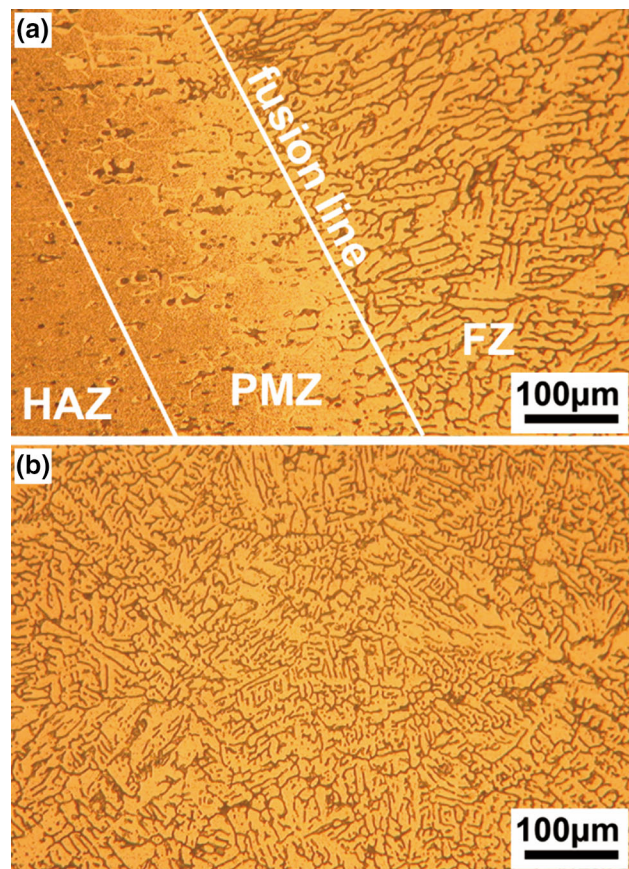

Fig. 8—OM images of the microstructure of joint 3: (a) area near to FZ edge and (b) FZ center.
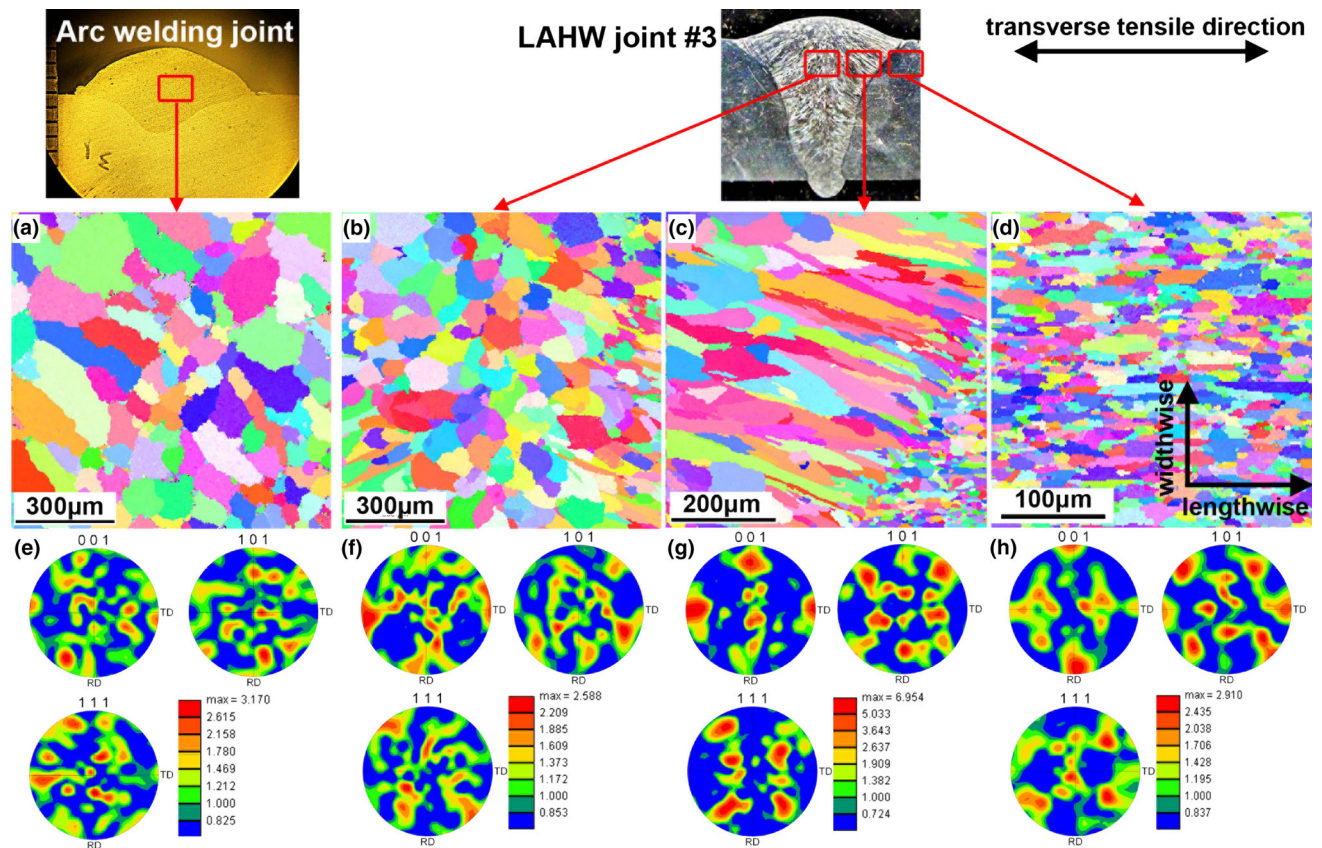
Fig. 9—EBSD images of the microstructure of joint 3: (*a*) IPF of arc welding joint, (*b*) IPF of equiaxed zone in the FZ, (*c*) IPF of columnar dendrite zone in the FZ, (*d*) IPF of overaging zone in the HAZ, (*e*) PF of arc welding joint, (*f*) PF of equiaxed zone in the FZ, (*g*) PF of columnar dendrite zone in the FZ, and (*h*) PF of overaging zone in the HAZ.

F. Strength Improvement Mechanism Depending on Laser-Arc Interaction

Lower heat input indicates that there would be an abnormal energy transfer in LAHW, which is different from that of pure laser welding and pure arc welding. This transfer causes less effective heat input absorbed by welding material, which refines grain size and weakens overaging effect. It will be discussed as follows.

Laser-arc interaction in the LAHW plays a big role in this abnormal energy transfer. During LAHW, laser-arc interaction can be divided into two parts. One is the effect of the laser on the arc, while the other is the effect of the arc on the laser. Because the compression effect of laser beam on arc improves the energy density of arc and increases the effective heat input,[40] it can be inferred that the laser-arc interaction decreases the effective heat input by reducing laser energy rather than arc energy. Then the effect of arc on the laser will play a part. This phenomenon is first reflected by the inverse bremsstrahlung absorption effect of the arc on the laser beam. Since the 1070-nm wavelength of a fiber laser beam leads to an extremely low absorption coefficient, the laser energy absorbed by the arc can be ignored.[41] In addition, lots of the laser beam transfers to BM by

the Fresnel effect in the laser-induced keyhole.[42] As is shown in Figure 11, the Fresnel effect is characterized by multiple reflections and absorptions on the keyhole wall and the variable keyhole profile will change this characteristic. Plasma flow force, arc pressure, molten drop impact force, and electromagnetic force generated by the MIG arc will inevitably vary the molten pool and then the keyhole profile.[43] As a result, the arc will influence the laser beam transfer. The schematic of this phenomenon is shown in Figure 12. The details are analyzed as follows.

First, the arc influences the laser beam transfer at the upper part of the keyhole directly. When the incident laser beam arrives at the upper part of the keyhole, it is reflected and absorbed first by the front wall of the keyhole. Usually the reflected beam will shine into the rear wall of the keyhole, as shown in Figure 11. But the large pit at the rear of the keyhole leads the laser beam out from the keyhole as shown in Figure 12, which makes the welding material absorb less laser energy.

Second, the arc also influences the laser beam transfer at the lower part of keyhole. The arc-induced pit on the surface of the melt pool reduces the depth of the keyhole so that the laser beam is easier to run through the
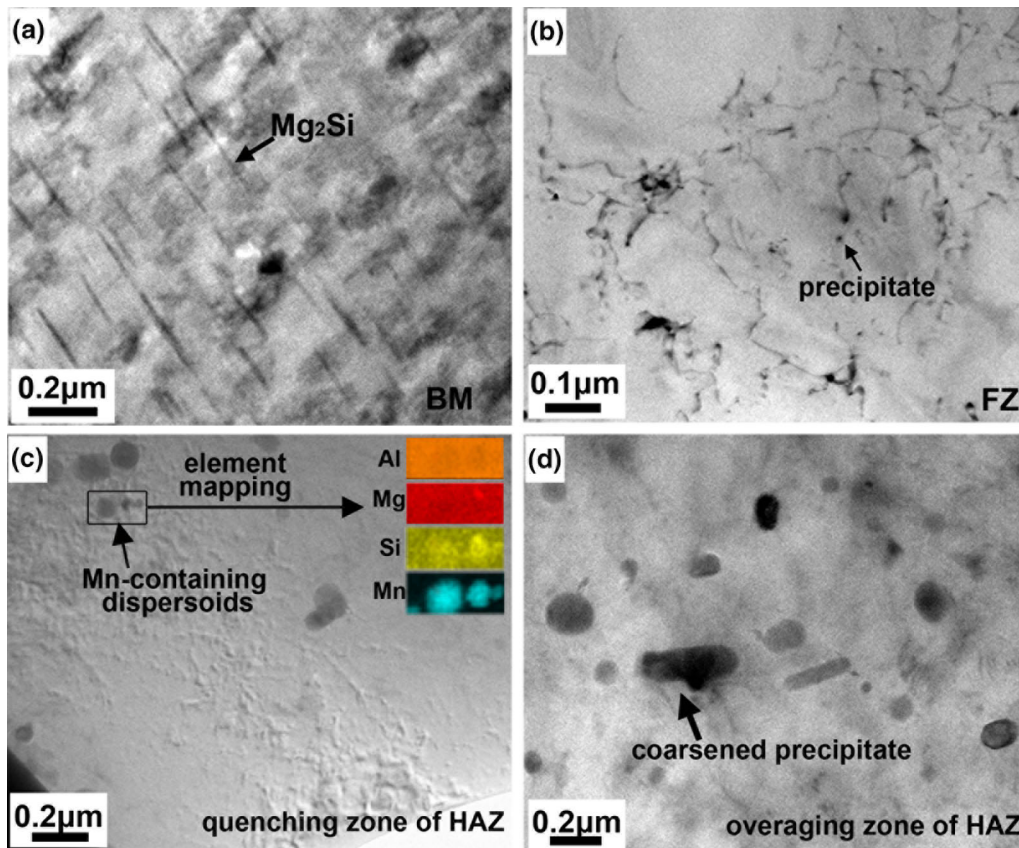
Fig. 10—Bright-field TEM micrographs of joint 3: (*a*) BM, (*b*) FZ, (*c*) quenching zone of HAZ, and (*d*) overaging zone of HAZ.

Table IV. Contributions of Different Strengthening Factors on the YS of LAHWed Joint 3

	Overaging Zone of HAZ				FZ	
	Value (MPa)		Percentage (pct)			
	Width	Length	Width	Length	Value (MPa)	Percentage (pct)
σ_0	10	10	4	5	10	4.7
σ_{HP}	96	50	39	25	44	20.5
σ_P	140	140	56	70	76	35.3
σ_{SS}	0	0	0	0	85	39.5
Total	246	200	100	100	215	100

keyhole. And the laser beam is also reflected to exit the keyhole by the wall at the bottom of the keyhole.

To investigate the laser energy intensity distribution in the keyhole, the feature of the Fresnel effect at the lower part of the keyhole is analyzed. The Fresnel absorptivity A can be calculated by the equation:[44]

$$A = 1 - \frac{1}{2}\left(\frac{1 + (1 - \varepsilon\cos\varphi)^2}{1 + (1 + \varepsilon\cos\varphi)^2} + \frac{\varepsilon^2 - 2\varepsilon\cos\varphi + 2\cos^2\varphi}{\varepsilon^2 + 2\varepsilon\cos\varphi + 2\cos^2\varphi}\right)$$
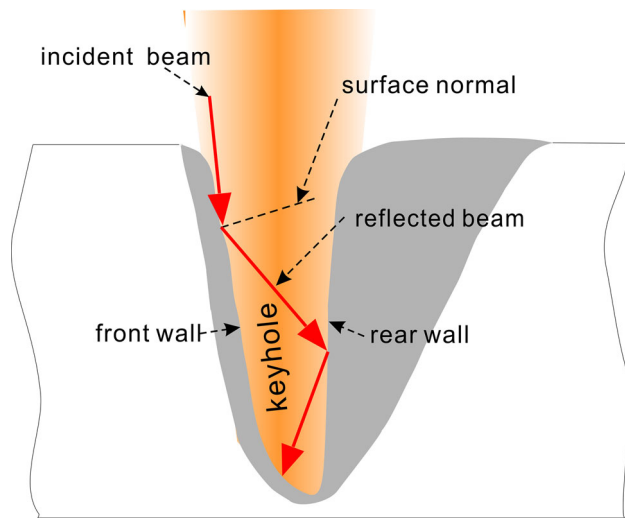
[5]

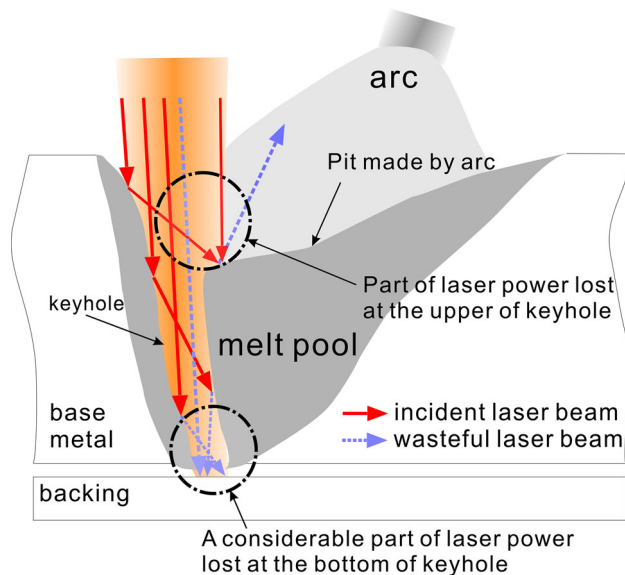Fig. 11—Schematic of Fresnel effect on the keyhole in laser welding.

Fig. 12—Loss mechanism of heat input during LAHW.

where the value of ε is related to the electrical conductance per unit depth of metal and φ is the angle between the incident ray and the surface normal. The smaller φ generates higher absorptivity. The observed keyhole profile is bent, and the big bent magnitude appears at the lower part of the keyhole[45,46] so the angle φ of this part is the smallest. According to the Fresnel absorptivity (Eq. [5]), very little laser energy distributes at the upper part of the keyhole and a majority of laser power is concentrated at the lower part of the keyhole, as shown in Figure 13.[45] It indicates that the majority of laser energy dissipates *via* the tip of the through keyhole. The deeper penetration in the backing of LAHW caused by the penetrated laser beam also proves that more laser power in LAHW escapes from the keyhole.

By this analysis, the depressed melt pool caused by the arc changes the keyhole morphology, which leads the majority of laser energy lost at the lower part of keyhole. Because the laser energy occupies a large proportion of the heat input, the great loss significantly reduces the heat input. Thus, it refines the grain size in the FZ of the LAHWed joint and weakens the overaging effect on HAZ. The finer grain enhances the FZ. The weak overaged precipitate maintains the high strength of HAZ.

IV. CONCLUSIONS

(1) The thick AA6082 Al alloy joint without defects was welded successfully by LAHW. The tensile strengths of the HAZ and the FZ of the LAHW joint were improved. The microstructure characteristics showed that the tensile strength enhancement of the LHAWed joint was attributed to finer grains, finer precipitates, and solid solution.

(2) The grain size of the LAHW joint was smaller than the arc welding joint with the same parameters for LAHW. There still were lots of Mg_2Si precipitates and Mn-containing dispersoids in the HAZ. These proved LHAW had a lower heat input.

(3) The arc made a large pit at the rear of the keyhole on the surface of the melt pool that leaded part of the laser energy out from the upper keyhole and the majority of the laser energy dissipated *via* the lower keyhole. The energy absorbed by the weld material *via* the keyhole wall was less, which reduced the heat input of LAHW. Low heat input refined the grain and weakened the overaging effect, which enhanced the strength of the LAHWed joint.
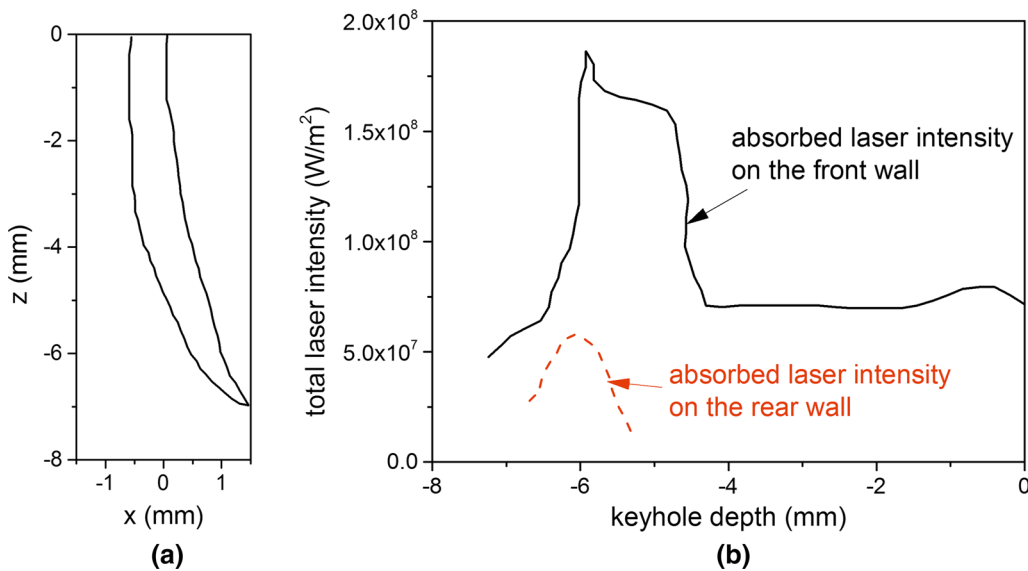
(a)   **(b)**

Fig. 13—Keyhole profile and its laser energy intensity distribution: (*a*) profile of the keyhole and (*b*) total laser intensity absorbed on the keyhole wall.

REFERENCES

1. P. Von Witzendorff, S. Kaierle, O. Suttmann, and L. Overmeyer: *Metall. Mater. Trans. A*, 2015, vol. 46, pp. 1678–88.
2. L. Wan, Y. Huang, W. Guo, S. Lv, and J. Feng: *J. Mater. Sci. Technol.*, 2014, vol. 30, pp. 1243–50.
3. Y. Ruan, X. Qiu, W. Gong, D. Sun, and Y. Li: *Mater. Des.*, 2012, vol. 35, pp. 20–4.
4. M. Cabibbo, A. Forcellese, M. El Mehtedi, and M. Simoncini: *Mater. Sci. Eng. A*, 2014, vol. 590, pp. 209–17.
5. T. Graf and H. Staufer: *Weld. J.*, 2003, vol. 82, p. 42.
6. P. Moore, D. Howse, and E. Wallach: *Sci. Technol. Weld. Join.*, 2004, vol. 9, pp. 314–22.
7. S. Katayama, S. Uchiumi, M. Mizutani, J. Wang, and K. Fujii: *Weld. Int.*, 2007, vol. 21, pp. 25–31.
8. C.T. Frank Vollertsen: *ICALEO 2005*, LIA, Florida, 2005, p. 506.
9. H. Yonetani: *Weld. Int.*, 2008, vol. 22, pp. 701–04.
10. J. Shen, L. Wen, Y. Li, and D. Min: *Mater. Sci. Eng. A*, 2013, vol. 578, pp. 303–9.
11. I. Tomashchuk, D. Grevey, and P. Sallamand: *Mater. Sci. Eng. A*, 2015, vol. 622, pp. 37–45.
12. M. Sheikhi, F. Malek Ghaini, and H. Assadi: *Sci. Technol. Weld. Join.*, 2014, vol. 19, pp. 250–55.
13. G. Cam and M. Kocak: *Int. Mater. Rev.*, 1998, vol. 43, pp. 1–44.
14. G. Casalino, M. Mortello, P. Leo, K.Y. Benyounis, and A.G. Olabi: *Mater. Des.*, 2014, vol. 61, pp. 191–98.
15. O. Ola and F. Doern: *Int. J. Adv. Manuf. Technol.*, 2015, vol. 80, pp. 3–10.
16. P.D. Lee and J.D. Hunt: *Acta Mater.*, 2001, vol. 49, pp. 1383–98.
17. M. Gao, H.-G. Tang, X.-F. Chen, and X.-Y. Zeng: *Mater. Des.*, 2012, vol. 42, pp. 46–54.
18. Z. Wang, M. Gao, H. Tang, and X. Zeng: *Mater. Charact.*, 2011, vol. 62, pp. 943–51.
19. C. He, C.X. Huang, Y.J. Liu, J.K. Li, and Q. Wang: *Mater. Des.*, 2015, vol. 65, pp. 289–96.
20. J. Yan, X. Zeng, M. Gao, J. Lai, and T. Lin: *Appl. Surf. Sci.*, 2009, vol. 255, pp. 7307–13.
21. Z. Gao, J. Fang, Y. Zhang, G. Ran, and S. Zhang: *Int. J. Electrochem. Sci.*, 2013, vol. 8, pp. 7905–17.
22. C. Zhang, M. Gao, G. Li, C. Chen, and X. Zeng: *Sci. Technol. Weld. Join.*, 2013, vol. 18, pp. 703–10.
23. B. Hu and I.M. Richardson: *Mater. Sci. Eng. A*, 2007, vol. 459, pp. 94–100.
24. S. Yan, H. Chen, Z. Zhu, and G. Gou: *Mater. Des.*, 2014, vol. 61, pp. 160–7.
25. G. Liu, G.J. Zhang, R.H. Wang, W. Hu, J. Sun, and K.H. Chen: *Acta Mater.*, 2007, vol. 55, pp. 273–84.
26. A. Alankar, I.N. Mastorakos, and D.P. Field: *Acta Mater.*, 2009, vol. 57, pp. 5936–46.
27. M. Crumbach, M. Goerdeler, and G. Gottstein: *Acta Mater.*, 2006, vol. 54, pp. 3291–3306.
28. S. Katayama, Y. Naito, S. Uchiumi, and M. Mizutani: *Trans. JWRI*, 2006, vol. 35, p. 13.
29. R. Kumar, U. Dilthey, D. Dwivedi, and P. Ghosh: *Mater. Des.*, 2009, vol. 30, pp. 306–13.
30. M. Ericsson and R. Sandström: *Int. J. Fatigue*, 2003, vol. 25, pp. 1379–87.
31. M. Scott and M. Gittos: *Weld. J.*, 1983, vol. 62, pp. 243s–52s.
32. L. Hector, Jr, Y.-L. Chen, S. Agarwal, and C. Briant: *Metall. Mater. Trans. A*, 2004, vol. 35, pp. 3032–38.
33. D.H. Lee, J.H. Park, and S.W. Nam: *Mater. Sci. Technol. Lond.*, 1999, vol. 15, pp. 450–55.
34. W. Woo, H. Choo, D.W. Brown, and F. Zhili: *Metall. Mater. Trans. A*, 2007, vol. 38, pp. 69–76.
35. G. Edwards, K. Stiller, G. Dunlop, and M. Couper: *Acta Mater.*, 1998, vol. 46, pp. 3893–3904.
36. Y.S. Sato, H. Kokawa, M. Enomoto, S. Jogan, and T. Hashimoto: *Metall. Mater. Trans. A*, 1999, vol. 30, pp. 3125–30.
37. C. Genevois, A. Deschamps, A. Denquin, and B. Doisneau-Cottignies: *Acta Mater.*, 2005, vol. 53, pp. 2447–58.
38. K. Kendig and D. Miracle: *Acta Mater.*, 2002, vol. 50, pp. 4165–75.
39. X. Feng, H. Liu, and S. Suresh Babu: *Scripta Mater.*, 2011, vol. 65, pp. 1057–60.

40. M. Gao, S. Mei, Z. Wang, X. Li, and X. Zeng: *J. Mater. Process. Technol.*, 2012, vol. 212, pp. 1338–46.
41. B. Hu and G. Den Ouden: *Sci. Technol. Weld. Join.*, 2005, vol. 10, pp. 76–81.
42. R. Fabbro, S. Slimani, F. Coste, and F. Briand: *J. Phys. D*, 2005, vol. 38, p. 1881.
43. Z. Gao, Y. Wu, and J. Huang: *Int. J. Adv. Manuf. Technol.*, 2009, vol. 44, pp. 870–79.
44. J.-H. Cho and S.-J. Na: *J. Phys. D.*, 2006, vol. 39, p. 5372.
45. X. Jin, L. Li, and Y. Zhang: *J. Phys. D.*, 2002, vol. 35, p. 2304.
46. Y. Cheng, X. Jin, S. Li, and L. Zeng: *Opt. Laser Technol.*, 2012, vol. 44, pp. 1426–36.